IEEE Access
Multidisciplinary ⋮ Rapid Review ⋮ Open Access Journal

Received April 8, 2022, accepted April 19, 2022, date of publication April 22, 2022, date of current version April 28, 2022.

Digital Object Identifier 10.1109/ACCESS.2022.3169618

Modified Proportionate Affine Projection Algorithm Based Adaptive DSTATCOM Control With Increased Convergence Speed

AROBINDA DASH[1], (Graduate Student Member, IEEE),
UTKAL RANJAN MUDULI[2], (Member, IEEE),
SURYA PRAKASH[1], (Graduate Student Member, IEEE),
KHALIFA AL HOSANI[2], (Senior Member, IEEE),
SANDHYA RANI GONGADA[3],
AND RANJAN KUMAR BEHERA[1], (Senior Member, IEEE)

[1]Department of Electrical Engineering, Indian Institute of Technology (IIT) Patna, Patna 801103, India
[2]Advanced Power and Energy Center, Department of Electrical Engineering and Computer Science, Khalifa University, Abu Dhabi, United Arab Emirates
[3]Department of Electrical and Electronics Engineering, Vasavi College of Engineering, Hyderabad 500089, India

Corresponding author: Utkal Ranjan Muduli (utkal.muduli@ku.ac.ae)

This work was supported by the Ministry of Human Resource Development and Ministry of Power, Government of India, through IMPRINT under Project F. No. 1-18/2015-TS-TS.I; in part by the Khalifa University under Award KKJRC-2019-Trans2; and in part by the Advanced Technology Research Council ASPIRE Virtual Research Institute (VRI) Program, Abu Dhabi, United Arab Emirates, under Award VRI20-07.

ABSTRACT The three-phase DSTATCOM is prone to higher dynamics due to grid disturbances. The proportionate affine projection algorithm (PAPA) is an adaptive filter that can be used for DSTATCOM control. In order to overcome the sluggish convergence speed of adaptive filters, PAPA is proposed in this paper. The convergence rate versus the steady-state error is a trade-off in conventional adaptive filters. However, the utilization of two adaptive filters in CSS-PAPA increases the convergence and decreases the steady-state error. The suggested filter has the advantage of having a lower computational cost than a standard adaptive filter. The proposed filter helps the inverter to work as a shunt compensator. The goal of the suggested controller is to adjust for reactive power and unity power factor during faulty conditions. The proposed DSTATCOM controller has undergone experimental validation in the laboratory.

INDEX TERMS Adaptive filter, current compensation, DSTATCOM, power quality, voltage source converter.

I. INTRODUCTION

Grid harmonics have received a lot of attention due to their ability to cause problems with power quality in both transmission and distribution systems. The increasing reliance on power electronic devices in everyday household equipment and industrial sectors has become a major source of power quality issues. As a result, both the client and the utility have paid a significant penalty. Power quality issues in a weak grid can be mitigated using passive filters [1], active filters [2], and hybrid filters [3]. However, because of their considerable size, resonance, fixed compensation, and aging impact, passive filters are not an appealing choice for industrial applications. As a result, researchers are gravitating toward active power filters (APF). When the primary objective is harmonic compensation existing in the utility induced by loads, the static var compensator (STATCOM) is known as APF [4]. The use of APFs improves the quality of grid power by compensating for reactive power, mitigating harmonics, and adjusting phase angles. This is achieved by connecting the APF in series or in parallel with the utility. Series APFs are used to compensate harmonic voltages, while parallel or shunt APFs

The associate editor coordinating the review of this manuscript and approving it for publication was Suman Maiti.

are used for harmonic current compensation [5]. The use of STATCOM at the distribution end can be referred to as distributed STATCOM (DSTATCOM). DSTATCOM can be considered as a controlled current source or as a controlled voltage source. Because DSTATCOM is operated as a controlled current source, it has gained popularity. However, the indirect current control approach for DSTATCOM has weak transient responsiveness.

DSTATCOM works by injecting harmonic and/or reactive compensating currents to the opposite phase to restore balanced sinusoidal source currents that are in phase with the supply voltages. Again, accurate estimation of reference currents is essential for precise harmonic compensation by DSTATCOM. To achieve the synchronization of the source current with the supply voltage, an effective extraction of the current harmonics drawn by the nonlinear load and a correct calculation of the supply frequency are required. As a result, a system that can efficiently perform the aforementioned duties is extremely desirable for DSTATCOM control. The DSTATCOM operates in voltage control mode (VCM) and current control mode (CCM). The point-of-common coupling (PCC) voltage is only improved in the VCM mode. However, in CCM mode, DSTATCOM is responsible for improving the quality of the current and voltages of the grid. The CCM mode operation of DSTATCOM can be analyzed both in the frequency domain and the time domain. The frequency domain has a slow response time and a significant calculation burden. However, the time-domain-based control strategy offers a fast response time and computational complexity. The component-based modified technique [6], synchronous reference theory (SRFT) [7], vector resonant controller [8], instantaneous reactive power theory (IRPT) [9], adaptive Volterra second-order filter [10], unified ADALINEs neural filter [11], Lyapunov function [12], adaptive synchronous extraction [13], predictive current control [14], and dual tree complex wavelet transform [15] are developed as effective and popular time domain controllers. In [16], a linear quadratic Gaussian servo controller is investigated that claims to offer a faster estimate of reference tracking.

Several researchers have investigated various adaptive control approaches. Those include adaptive repetitive control [17], Gauss-Newton-based enhanced equal current approach [18], predictive current control [14], and Wiener filter [19]. Adaptive control strategies have the capability of updating their parameters as a result of disturbances in the system. There are some weight-based approaches that include adaptive recursive inverse [20], neural network-based adaptive control approach [21], frequency-adaptive fractional order repetitive control [22], affine projection-like algorithm [23], and echo state-based control techniques [24]. However, the LMS algorithm [25] only updates the weights based on a single input vector.

This paper proposes a combined step-size (CSS) proportionate affine projection algorithm (PAPA) to calculate the fundamental grid currents from distorted and imbalanced load currents. The goal of separation of the major components of the grid is to provide only the real power load requirements of the grid, while DSTATCOM provides the oscillating real power combined with the reactive power requirements of the linked load. In its intended application, the proposed system is used for harmonic suppression, excessive reactive power control, and load balancing in two modes, namely, power factor improvement and PCC voltage regulation. CSS-PAPA control strategy is preferable to the affine projection algorithm (APA) control strategy in applications where the input signals are highly correlated. As a result, the APA method is prone to slow convergence, which deteriorates depending on the nature of the input signal. This paper comprises the following contributions.

- The CSS-PAPA is proposed by merging adaptive LMS filters to address the issues that are frequently encountered with APA and its derivatives.
- Because of the many input vectors, the proposed approach offers the advantage of quickly calculating and dynamically updating weights.
- The suggested method is intended to be an efficient controller for achieving shunt compensation through DSTATCOM.
- The suggested technique also has the advantage of using a coefficient vector approach and having a rapid convergence speed regardless of the characteristics of the input signal.

Section II discusses the description and control of the DSTATCOM system with CSS-PAPA. However, a discussion of the results is provided in Section III. The final section, Section IV, provides a conclusion.

II. DSTATCOM CONTROL METHODOLOGY

A. SYSTEM DESCRIPTION

The three-phase grid supplies power to a three-phase nonlinear load with RL load. These nonlinear loads are the reason for nonlinear grid currents. To overcome these nonlinear effects along with reactive power compensation, a three-phase DSTATCOM is connected to a three-phase power grid at the point of common coupling (PCC), as shown in Fig. 1. The DSTATCOM is built with a three-phase voltage source converter (VSC) and a DC-link capacitor is installed on its DC side. To decrease the switching noise produced by insulated gate bipolar transistor (IGBT) switches, three-phase inductor filters are coupled with DSTATCOM at PCC. In the laboratory, a scaled prototype is developed and the CSS-PAPA algorithm-based control is validated under a range of load variations.

B. CONTROL STRUCTURE OF CSS-PAPA

Initially, the framework of the PAPA is developed, which forms the basis of our further derivations. Let $\hbar_{opt}$ be the unknown impulse response vector of the plant and $\psi^{(i)}$ be the

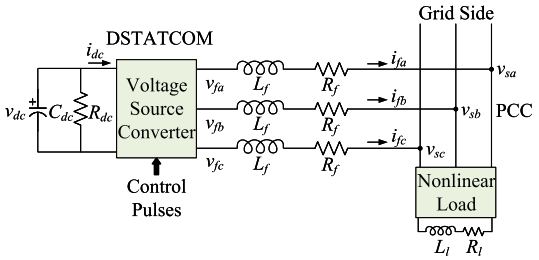

FIGURE 1. Topological configuration of grid integrated DSTATCOM.

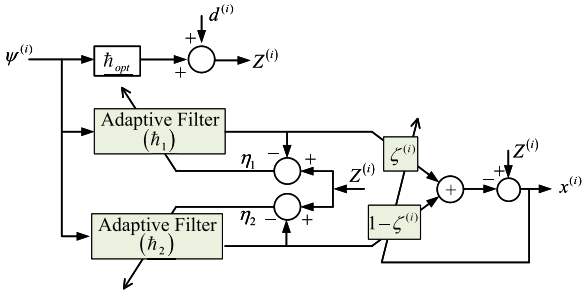

FIGURE 2. Schematic diagram of CSS-PAPA.

input signal vector of the adaptive filter as [23], [25], [26].

$$\hbar_{opt}^{(i)} = \left[\hbar_0^{(i)}, \hbar_1^{(i)}, \ldots, \hbar_{N-1}^{(i)}\right]^T \tag{1}$$

$$\psi^{(i)} = \left[\psi^{(i)}, \psi^{(i-1)}, \cdots \psi^{(i-k+1)}\right] \tag{2}$$

where N is the length of the adaptive filter and i denotes the present sample. From Fig. 2, the observed signal ($Z^{(i)}$) with additional impulsive noise ($d^{(i)}$) can be calculated as (3).

$$Z^{(i)} = \hbar_{opt}\left(\psi^{(i-1)}\right)^T + d^{(i)} \tag{3}$$

The estimated posterior is carried out on the output of the unknown system, and of the adaptive filter is

$$\eta_{opt} = Z^{(i)} - \left(\psi^{(i)}\right)^T \hbar^{(i)} \tag{4}$$

where $\hbar^{(i)}$ is calculated from $\hbar_{opt}^{(i)}$ after every iteration. The new update weight coefficient vector of PAPA can be obtained as (5).

$$\hbar^{(i)} = \hbar^{(i-1)} + \tau\psi^{(i)}G^{(i)}\left[\left(\psi^{(i)}\right)^T\psi^{(i)}G^{(i)} + \delta\mathbf{I}\right]^{-1}\eta^{(i)} \tag{5}$$

where τ is the step size of the iteration, $G^{(i)}$ $(= diag\left[g_0^{(i)}, g_1^{(i)}, \ldots, g_{N-1}^{(i)}\right])$ is the gain controlling matrix and $\mathbf{I}$ is an $N \times N$ identity matrix. The individual gain unit $(g_k^{(i-1)}, k \in \{0, \ldots, N-1\})$ can be written as (6).

$$g_k^{(i-1)} = \frac{Nx_k^{(i-1)}}{\sum_{k=0}^{N-1} x_k^{(i-1)}} \tag{6}$$

where $x_k^{(i-1)} = max\left\{p\, max\left\{q\left|\hbar_{opt}^{(i)}\right|\right\}, \left|\hbar_k^{(i-1)}\right|\right\}$. The initialization process requires the usage of the parameter p, which prevents the weight coefficients from stalling during updates when all the weight coefficients are set to zero at the start of the process. Similarly, the parameter q is a modest positive number that prevents $\hbar_{N-1}^{(i)}$ from stalling even though its value is significantly lower than the maximum coefficient. A larger step size τ_1 and the smallest step size τ_2 are observed during the iteration process and satisfy the relation $0 \leq \tau_2 \leq \tau_1$. The weight coefficient vector $\hbar^{(i-1)}$ is modified as $\hbar_1^{(i)}$ and $\hbar_2^{(i)}$ by taking into account these two different step sizes, given in (7)-(8).

$$\hbar_1^{(i)} = \hbar^{(i-1)} + \tau_1\psi^{(i)}G^{(i)}\left[\left(\psi^{(i)}\right)^T\psi^{(i)}G^{(i)} + \delta\mathbf{I}\right]^{-1}\eta^{(i)} \tag{7}$$

$$\hbar_2^{(i)} = \hbar^{(i-1)} + \tau_2\psi^{(i)}G^{(i)}\left[\left(\psi^{(i)}\right)^T\psi^{(i)}G^{(i)} + \delta\mathbf{I}\right]^{-1}\eta^{(i)} \tag{8}$$

These new two weight vectors $\hbar_1^{(i)}$ and $\hbar_2^{(i)}$ are organized by a variable mixing factor $\zeta^{(i)}$ with constraint $0 \leq \zeta^{(i)} \leq 1$ to form a new update weight vector as (9).

$$\hbar^{(i)} = \zeta\hbar_1^{(i)} + (1-\zeta^{(i)})\hbar_2^{(i)} \tag{9}$$

Substituting (7)-(8) into (9), the derived new equation of the weight coefficient vector as (10).

$$\lambda^{(i)} = \zeta^{(i)}\lambda_1 + (1-\zeta^{(i)})\lambda_2 \tag{10}$$

where $\lambda^{(i)}$ is called combined-step-size and its range varies from λ_1 to λ_2. The variable mixing factor τ is defined as the output of a sigmoid activation function with respect to a variable $\beta^{(i)}$ and can be derived as (11).

$$\tau^{(i)} = sgn[\beta^{(i)}] = \frac{1}{1+e^{-\beta^{(i)}}} \tag{11}$$

Here τ is calculated at each iteration minimizing the L_1-norm of the system output error $\eta^{(i)} = Z^{(i)} - \left(\psi^{(i)}\right)^T\hbar^{(i-1)}$ according to the following stochastic gradient descent rule where D is a positive value, and it is always greater than 1. To ensure the robustness of the algorithm in the presence of non-Gaussian impulsive interference, $\beta^{(i)}$ has been updated utilizing the gradient descent method to optimize the L_1-norm of the system error $\eta^{(i)} = Z^{(i)} - \left(\psi^{(i)}\right)^T\hbar^{(i-1)}$. Combining (9) and (10), the updated $\hbar^{(i)}$ can be derived as (12), shown at the bottom of the next page. Here, τ_β represents the step size of the adaption $\beta^{(i)}$ and D_1 is a positive value to prevent the simulation from stopping when $\zeta(i)$ becomes 0 or 1. The goal of the CSS-PAPA algorithm is to identify the true system impulse response $\hbar^{(i)}$ from the input signal $\psi^{(i)}$ and the desired output signal $x(i)$. Because the variable mixing factor is defined as the output of the sigmoid activation function (13), as shown at the bottom of the next page, which actually restricts the variable mixing factor to lie within the open interval (0,1). Now, the updated $\tau^{(i)}$ can

be derived as (14).

$$\tau^{(i)}=\begin{cases}1, & \text{if } \beta^{(i)} > -\ln\dfrac{D+1}{D-1}\\ 0, & \text{if } \beta^{(i)} < \ln\dfrac{D+1}{D-1}\\ \dfrac{D}{1+e^{\tau^{(i)}}}-\dfrac{D}{2}+0.5, & \text{otherwise}\end{cases} \tag{14}$$

where $\tau^{(i)} = \text{sgn}[\beta^{(i)}]$. To prevent the simulation from stopping while $\tau^{(i)}$ is equal to 1 or 0, (14) can be modified by adding a small positive value to it.

C. PROPOSED DSTATCOM CONTROL STRUCTURE

The control structure of grid integrated DSTATCOM by using CSS-PAPA algorithm is shown in Fig. 3. The load currents (i_{La}, i_{Lb}, i_{Lc}), the PCC line voltages (V_{sab}, V_{sbc}) and DC-link voltage ($V_{dcactual}$) are sensed as feedback signals. The sensed PCC line voltages are used to estimate the phase voltages (v_{sa}, v_{sb}, v_{sc}) as (15).

$$\begin{bmatrix}v_{sa}\\ v_{sb}\\ v_{sc}\end{bmatrix}=\frac{1}{3}\begin{bmatrix}2 & 1\\ -1 & 1\\ -1 & -2\end{bmatrix}\begin{bmatrix}v_{sab}\\ v_{sbc}\end{bmatrix} \tag{15}$$

Again, the phase voltages are used to generate positive sequence voltages (v_{pa}, v_{pb}, v_{pc}) of the distorted grid as (16).

$$\begin{bmatrix}v_{pa}\\ v_{pb}\\ v_{pc}\end{bmatrix}=\begin{bmatrix}1 & \alpha^2 & \alpha\\ \alpha & 1 & \alpha^2\\ \alpha^2 & \alpha & 1\end{bmatrix}\begin{bmatrix}v_{sa}\\ v_{sb}\\ v_{sc}\end{bmatrix} \tag{16}$$

where $\alpha = 1\angle 120°$ and $\alpha^2 = 1\angle 240°$ are complex operators. These PCC positive sequence voltages are used to estimate a direct unit template (u_{pa}, u_{pb}, u_{pc}) as (17).

$$u_{px}=\frac{1}{v_t}v_{px}, \quad x\in\{a,b,c\} \tag{17}$$

where v_t represents the amplitude of the terminal voltage and can be deduced as (18).

$$V_t = 0.816\sqrt{u_{pa}^2+u_{pa}^2+u_{pa}^2} \tag{18}$$

Again, the quadrature unit templates (u_{qa}, u_{qb}, u_{qc}) can be estimated from the direct unit templates, as (19).

$$\begin{bmatrix}u_{qa}\\ u_{qb}\\ u_{qc}\end{bmatrix}=\frac{1}{2\sqrt{3}}\begin{bmatrix}0 & -2 & 2\\ 3 & 1 & -1\\ -3 & 1 & -1\end{bmatrix}\begin{bmatrix}u_{pa}\\ u_{pb}\\ u_{pc}\end{bmatrix} \tag{19}$$

The updated weight in (12) is modified to weighted values corresponding to the active power components, and the reactive components are generated as (20).

$$\hbar_{px}{}^{(i)} = \hbar_{px}{}^{(i-1)}+\frac{\left[\zeta^{(i)}\tau_1+\left(1-\zeta^{(i)}\right)\tau_2\right]}{\left[\left(\psi_{px}^{(i)}\right)^T G^{(i)}\psi_{px}{}^{(i)}+\delta\mathbf{I}\right]^{-1}}\eta_x{}^{(i)} \tag{20}$$

$$\hbar_{qx}{}^{(i)} = \hbar_{qx}{}^{(i-1)}+\frac{\left[\zeta^{(i)}\tau_1+\left(1-\zeta^{(i)}\right)\tau_2\right]}{\left[\left(\psi_{qx}^{(i)}\right)^T G^{(i)}\psi_{qx}{}^{(i)}+\delta\mathbf{I}\right]^{-1}}\eta_x{}^{(i)} \tag{21}$$

The average per phase fundamental active weight component ($\hbar_{lp}$) is calculated from (20) as (22). The reactive weight component ($\hbar_{lq}$) can also be calculated as (23).

$$\hbar_{lp} = \frac{1}{3}\sum_{x\in\{a,b,c\}}\hbar_{px} \tag{22}$$

$$\hbar_{lq} = \frac{1}{3}\sum_{x\in\{a,b,c\}}\hbar_{qx} \tag{23}$$

For the operation of the unity power factor (UPF), the grid must deliver the fundamental component of the load current. The output of the proportional integral (PI) controller at the DC-link voltage of VSC is considered as the loss current (I_{loss}) to meet its power loss. A small amount of real average power ($\hbar_{cploss}$) must be drawn continuously from the grid to supply both switching loss and ohmic losses in the PWM converter. By equating the reference value of the DC link voltage (V_{dc}^*) and actual DC-link voltage (V_{dc}), the loss parameter of the VSC is calculated. This signal is passed through a PI controller, which is termed the loss component

$$\begin{aligned}\hbar^{(i)} &= \zeta^{(i)}\hbar_1{}^{(i)}+\left(1-\zeta^{(i)}\right)\hbar_2{}^{(i)} = \hbar^{(i-1)}+\frac{\zeta^{(i)}\tau_1\psi^{(i)}G^{(i)}\eta^{(i)}}{\left[\left(\psi^{(i)}\right)^T\psi^{(i)}G^{(i)}+\delta\mathbf{I}\right]}+\left(1-\zeta^{(i)}\right)\frac{\tau_2\psi^{(i)}G^{(i)}\eta^{(i)}}{\left[\left(\psi^{(i)}\right)^T\psi^{(i)}G^{(i)}+\delta\mathbf{I}\right]}\\ &= \zeta^{(i)}\left[\hbar^{(i-1)}+\frac{\tau_1\psi^{(i)}G^{(i)}\eta^{(i)}}{\left[\left(\psi^{(i)}\right)^T\psi^{(i)}G^{(i)}+\delta\mathbf{I}\right]}\right]+\left(1-\zeta^{(i)}\right)\left[\hbar^{(i-1)}+\frac{\tau_2\psi^{(i)}G^{(i)}\eta^{(i)}}{\left[\left(\psi^{(i)}\right)^T\psi^{(i)}G^{(i)}+\delta\mathbf{I}\right]}\right]\\ &= \hbar^{(i-1)}+\frac{\lambda\psi^{(i)}G^{(i)}\eta^{(i)}}{\left[\left(\psi^{(i)}\right)^T\psi^{(i)}G^{(i)}+\delta\mathbf{I}\right]}\end{aligned} \tag{12}$$

$$\begin{aligned}\beta^{(i)} &= \beta^{(i-1)}-\tau_\beta\frac{\partial\mid\eta^{(i)}\mid}{\partial\beta^{(i-1)}} = \beta^{(i-1)}+\tau_\beta\left(\psi^{(i)}\right)^T\frac{\partial\hbar^{(i-1)}}{\partial\beta^{(i-1)}}\text{sgn}\left(\eta^{(i)}\right)\\ &= \beta^{(i-1)}+\tau_\beta\left(\psi^{(i)}\right)^T(\tau_1-\tau_2)\frac{\partial\zeta^{(i-1)}}{\partial\beta^{(i-1)}}\left[\psi^{(i-1)}G^{(i-1)}\right]\left[\left(\psi^{(i-1)}\right)^T\psi^{(i-1)}G^{(i-1)}+\delta\mathbf{I}\right]^{-1}\eta^{(i-1)}\text{sgn}\left(\eta^{(i)}\right)\\ &= \beta^{(i-1)}+\tau_\beta(\tau_1-\tau_2)\zeta^{(i-1)}(1-\zeta^{(i-1)})\left[\left(\psi^{(i)}\right)^T\psi^{(i-1)}G^{(i-1)}\right]\left[\psi^{(i-1)}\psi^{(i-1)}G^{(i-1)}+\delta\mathbf{I}\right]^{-1}\eta^{(i-1)}\text{sgn}\left(\eta^{(i)}\right)\end{aligned} \tag{13}$$

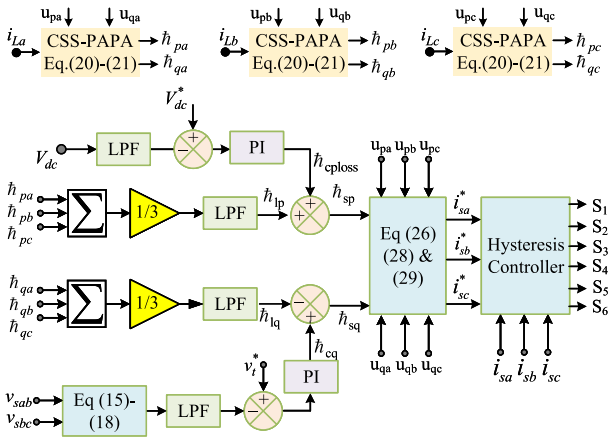

FIGURE 3. CSS-PAPA based control algorithm for DSTATCOM.

required to maintain the DC-link voltage to its reference value and is calculated as (24).

$$\hbar_{cploss}^{(i)} = \hbar_{cploss}^{(i-1)} + K_p[V_{err}^{(i)} - V_{err}^{(i-1)}] + K_i V_{err}^{(i)} \tag{24}$$

where $V_{err}^{(i)}$ $(= V_{dc}^{*} - V_{dc})$ represents the error in the voltage of the DC link. The active reference grid currents are calculated as (25).

$$\hbar_{sp} = \hbar_{lp} + \hbar_{cploss} \tag{25}$$

The active component of the reference grid current is calculated as (26).

$$i_{px}^{*} = \hbar_{sp} u_{px}, \quad x \in \{a, b, c\} \tag{26}$$

Here it can be noted that the reference grid current should be in phase with the grid current with no zero-sequence component. The DC link voltage is observed to be 1.6 to 2 times the peak of the source voltage. In this range, %THD of the grid current is achieving the minimum value. In general, the filter current flows from the inverter terminal to the PCC terminal, that is, from high potential to low potential. Therefore, the DC-link terminal voltage is kept at a higher value than the PCC voltage.

For zero voltage regulation (ZVR), the source must deliver the same direct axis component along with the sum of the quadrature axis current ($\hbar_{sq}$). As mentioned in (27), net weight of the reactive component of the reference three-phase grid current ($\hbar_{sq}$) can be obtained from the difference of $\hbar_{cq}$ and $\hbar_{lq}$ to regulate the PCC grid voltage. $\hbar_{lq}$ can be obtained from (23), while $\hbar_{cq}$ is obtained from the output of the terminal voltage tracking regulator (PI controller). The amplitude of the ac terminal voltage (V_t) in the PCC is controlled to its reference voltage (V_t^{*}) using the PI-based tracking controller. Here, K_{pt} and K_{it} are the proportional and integral gains of this PI controller, which are tabulated in Table 1.

$$\hbar_{sq} = \hbar_{cq} - \hbar_{lq} \tag{27}$$

The reactive component of the reference grid current is calculated as (28).

$$i_{qx}^{*} = u_{qx}\hbar_{sq}, \quad x \in \{a, b, c\} \tag{28}$$

Therefore, the grid reference currents are calculated as (29).

$$i_{sx}^{*} = i_{px}^{*} + i_{qx}^{*}, \quad x \in \{a, b, c\} \tag{29}$$

The VSC gate pulses are initiated by the hysteresis current controller (HCC) [31]–[33]. Several other switching schemes are available in the literature that include stationary reference frame ($\alpha\beta$-frame) enabled space vector modulation (SVM) scheme [34], model predictive control [35], direct power control [36], and sinusoidal PWM scheme in *abc*-frame [37]. However, the HCC method is faster irrespective of several disadvantages such as higher switching frequencies, variable switching frequencies, etc., [38]. The hysteresis band of ($\delta = 0.01$) is selected for the appropriate operation of the proposed controller. The error is generated by reducing the sensed grid current (i_{sa}, i_{sb}, i_{sc}) from the grid reference currents ($i_{sa}^{*}, i_{sb}^{*}, i_{sc}^{*}$).

D. CONTROLLER PARAMETER SELECTION

The DSTATCOM is injecting power to grid through a line filter and its parameters are mentioned in Table 1. Those details are analyzed in detail as the following.

1) SELECTING OF DC-LINK VOLTAGE

The minimum DC-link voltage of the three-phase inverter should be greater than twice the peak of the ac-phase voltage of the grid. The DC-link voltage v_dc is estimated as (30).

$$v_{dc} > 1.6 m_a v_{sab} \tag{30}$$

where m_a is the modulation index with the selected minimum value of v_{dc} at $160V$.

2) SELECTING THE PAPA PARAMETERS

Fig. 4 shows the curves of the sigmoid activation function 11, whose modification is provided in 14. By equating 11 and 14, the value of D can be obtained as '1'. According to Fig. 2, the combined step size $\lambda^{(i)} = \zeta^{(i)}\lambda_1 + (1 - \zeta^{(i)})\lambda_2$ with 14 can rapidly switch from the large step size λ_1 to the small step size of λ_2. Therefore, the proposed CSS-PAPA quickly achieves low steady-state maladjustment of the PAPA with a small step size λ_2.

3) K_p AND K_i DESIGN FOR OUTER LOOP AND DECIDING LPF BANDWIDTH

The open loop transfer function of the DC-link voltage regulation loop, shown in Fig.5, is described as (31). This technique utilizes a feed-forward term P_{ff}, which stabilizes the PI controller with better accuracy during integration offset and saturation overflow.

$$G_{dc}(s) = \left(K_p + \frac{K_i}{s}\right)\left(\frac{1}{C_{dc}}\right) \tag{31}$$

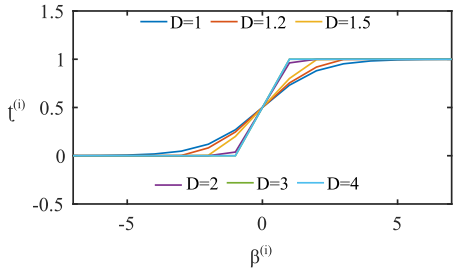

FIGURE 4. Sigmoid function curves of (11) and (14) with variation of *D*.

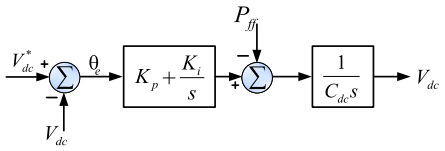

FIGURE 5. Transfer function of the DC-link voltage regulation.

The corresponding second-order closed-loop transfer function ($G_c(s)$) can be expressed as (32).

$$G_c(s) = \frac{G_{dc}(s)}{1 + G_{dc}(s)} \tag{32}$$

Here, the characteristic polynomial can be denoted as (33).

$$1 + G_{dc}(s) = s^2 + \underbrace{(K_p C_{dc}^{-1})}_{2\xi\omega_c} s + \underbrace{(K_i C_{dc}^{-1})}_{\omega_c} \tag{33}$$

where ξ denotes the damping factor and ω_{dc} represents the bandwidth of the outer loop. Now, the PI controller gains K_p and K_i can be simplified as (34).

$$\begin{aligned} K_p &= 2C_{dc}\xi\omega_{dc} \\ K_i &= C_{dc}\omega_{dc}^2 \end{aligned} \tag{34}$$

To achieve a good compromise between dynamic and less settling time, the value of the damping ratios ξ must be set to 0.707. The bandwidth frequency that gives the phase margin varies between 45° and 65°. For a fast and stable response, the bandwidth frequency is equal to 433 rad/s, and the phase margin is obtained as 64°. The K_p and K_i corresponding to the selected bandwidth frequency are 0.98 and 200, respectively. It is found that a second harmonic oscillation occurs during the grid converter startup, as well as in the unbalanced grid conditions that cause the DC voltage to oscillate. With the help of the low-pass filter (LPF), the oscillation of the dc-link voltage can be reduced. The low-pass filter is set to have its effective cutoff frequency set at five times the grid frequency. The problem with this approach is that it introduces a delay into the system, which limits the bandwidth of the controller.

III. EXPERIMENTAL VALIDATION AND DISCUSSION

To feed nonlinear loads, a weak grid was considered in this work. The issue of power quality in this weak grid has been investigated and a proper solution based on the proposed algorithm has been proposed. The suggested DSTATCOM control algorithm is used to solve power quality concerns. Initially, a simulation is performed using MATLAB/Simulink and the results are depicted in Fig. 7. In the laboratory, an experimental prototype of DSTATCOM is being developed to test the control algorithm, as shown in Fig. 6. It is made up of a three-phase VSC, interface inductors, and a nonlinear load based on a three-phase diode bridge rectifier. The control technique is implemented using a digital signal processor (DSP) dSPACE 1202 with eight analog-to-digital converter (ADC) channels. The voltage and current signals are sensed by a Hall effect voltage (LEM LV 25P) and a current transducer (LEM LA 55P) in the experimental prototype. In the experimental setting, the voltage is reduced from 500 V to 5 V, and a current of 10 A in the power grid

TABLE 1. Experimental prototype parameters.

System quantities	Values
Source voltage (rms)	$40 \pm 5\%$ V L-N, f=50 Hz
Line filter	R_f = 1.32 Ω, L_f = 3.54 mH
Non-linear load	3-Φ rectifier with RL load of 4 Ω, 40 mH
PI tuning parameters	K_{pt} = 0.152, K_{it} = 168, K_p = 0.98, K_i = 200
DSTATCOM parameters	V_{dc}^* = 160 V, C_{dc} = 2200 μF, D=1

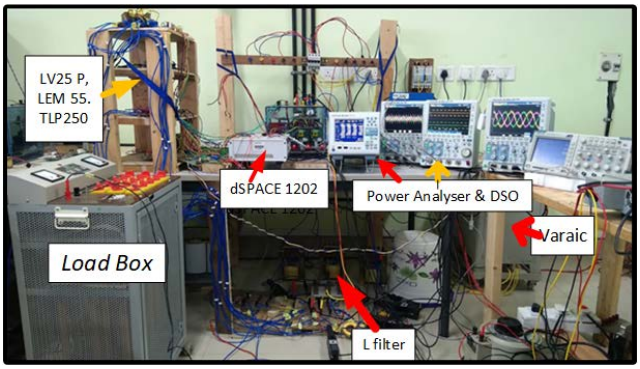

FIGURE 6. Experimental setup with DSTATCOM prototype.

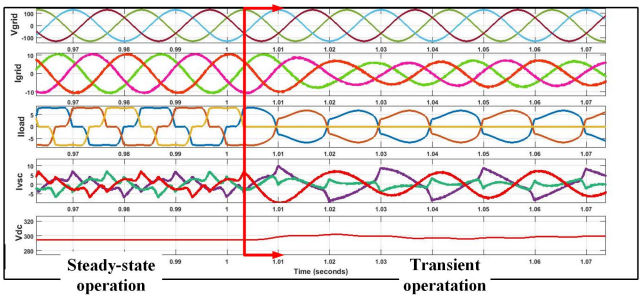

FIGURE 7. Simulation result during steady state and transient state.

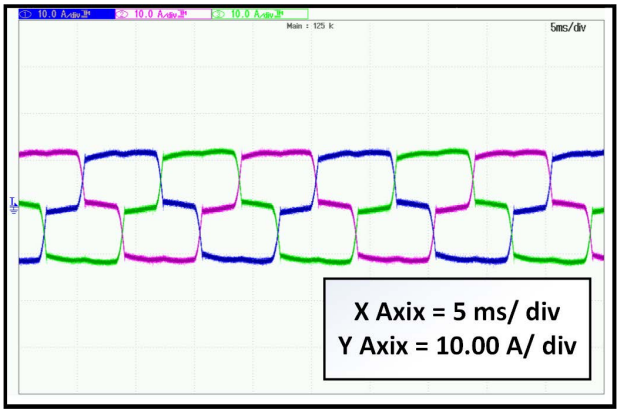

(a)

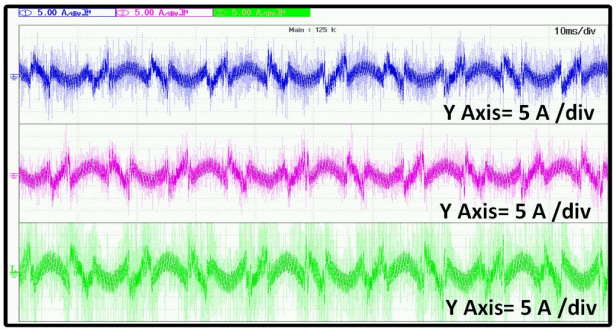

(b)

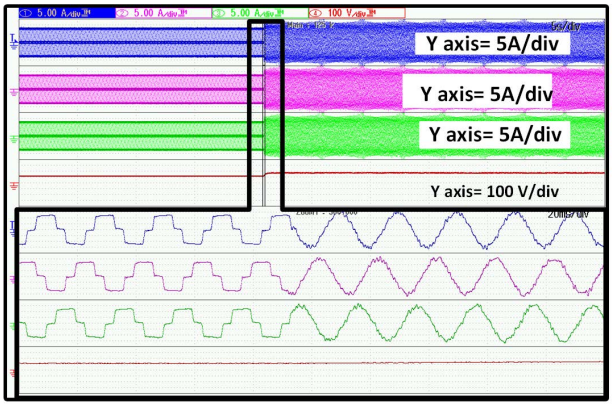

(c)

FIGURE 8. Nonlinear characteristic of (a) load current, (b) Compensation current flow from DSTATCOM, and (c) grid current with the operation of DSTATCOM at steady state condition.

is converted to 5 V using the transducers described above. For the control of VSI-based DSTATCOM, the proposed control method is constructed using dSPACE 1102. Stable-state and transient-state waveforms were recorded using a four-channel YOKOGAWA DSO-DLM2024 power analyzer and a four-channel YOKOGAWA DSO-DLM2024 digital storage oscilloscope. During these tests, the DC-link voltage of DSTATCOM kept constant at the reference value. The RMS value of the source voltage (phase-ground) in this case is 41 V, and the control algorithm in the DSP generates

PLL U1
Freq 49.993 Hz
Urms1 41.20 V
Irms1 9.65 A
P1 0.384kW
S1 0.397kVA
Q1 0.101kvar
λ1 0.9670
ϕ1 14.76 °
Uthd1 5.675 %
Ithd1 19.485 %
Pthd1 0.020 %
PAGE 1/5

Or.	I1 [A]	hdf[%]	Or.	I1 [A]	hdf[%]
Tot.	9.65		dc	-0.02	-0.249
1	9.47	98.083	2	0.04	0.373
3	0.11	1.094	4	0.04	0.396
5	1.54	15.991	6	0.02	0.247
7	0.98	10.136	8	0.03	0.262
9	0.08	0.797	10	0.02	0.236
11	0.33	3.378	12	0.01	0.125
13	0.24	2.507	14	0.01	0.085
15	0.03	0.303	16	0.01	0.082
17	0.07	0.744	18	0.01	0.055
19	0.06	0.650	20	0.00	0.023
21	0.01	0.106	22	0.00	0.039
23	0.02	0.197	24	0.00	0.016
25	0.02	0.199	26	0.00	0.006
27	0.00	0.037	28	0.00	0.012
29	0.01	0.059	30	0.00	0.003
31	0.01	0.073	32	0.00	0.005
33	0.00	0.015	34	0.00	0.014
35	0.00	0.022	36	0.00	0.009
37	0.00	0.024	38	0.00	0.007
39	0.00	0.012	40	0.00	0.007

(a)

PLL U1
Freq 49.975 Hz
Urms2 39.20 V
Irms2 9.31 A
P2 0.352kW
S2 0.365kVA
Q2 0.096kvar
λ2 0.9651
ϕ2 15.18 °
Uthd2 5.997 %
Ithd2 20.606 %
Pthd2 0.076 %
PAGE 2/5

Or.	I2 [A]	hdf[%]	Or.	I2 [A]	hdf[%]
Tot.	9.31		dc	-0.00	-0.027
1	9.11	97.854	2	0.02	0.263
3	0.15	1.599	4	0.02	0.208
5	1.65	17.746	6	0.00	0.032
7	0.85	9.102	8	0.02	0.200
9	0.10	1.059	10	0.01	0.156
11	0.39	4.226	12	0.00	0.020
13	0.18	1.922	14	0.01	0.091
15	0.04	0.398	16	0.00	0.050
17	0.09	0.984	18	0.00	0.013
19	0.04	0.423	20	0.00	0.025
21	0.01	0.151	22	0.00	0.029
23	0.02	0.264	24	0.00	0.002
25	0.01	0.097	26	0.00	0.013
27	0.01	0.062	28	0.00	0.008
29	0.01	0.089	30	0.00	0.008
31	0.00	0.023	32	0.00	0.000
33	0.00	0.025	34	0.00	0.006
35	0.00	0.031	36	0.00	0.008
37	0.00	0.011	38	0.00	0.006
39	0.00	0.014	40	0.00	0.005

(b)

PLL U1
Freq 49.962 Hz
Urms3 39.64 V
Irms3 9.37 A
P3 0.358kW
S3 0.372kVA
Q3 0.100kvar
λ3 0.9633
ϕ3 15.58 °
Uthd3 5.570 %
Ithd3 20.285 %
Pthd3 0.005 %
PAGE 3/5

Or.	I3 [A]	hdf[%]	Or.	I3 [A]	hdf[%]
Tot.	9.37		dc	0.03	0.312
1	9.18	97.921	2	0.05	0.509
3	0.05	0.523	4	0.04	0.436
5	1.60	17.075	6	0.03	0.367
7	0.92	9.830	8	0.03	0.353
9	0.01	0.063	10	0.02	0.247
11	0.36	3.886	12	0.02	0.200
13	0.22	2.385	14	0.01	0.154
15	0.00	0.046	16	0.01	0.058
17	0.09	0.947	18	0.01	0.063
19	0.06	0.607	20	0.01	0.067
21	0.00	0.014	22	0.00	0.035
23	0.02	0.253	24	0.00	0.029
25	0.02	0.183	26	0.00	0.023
27	0.00	0.023	28	0.00	0.011
29	0.01	0.095	30	0.00	0.017
31	0.01	0.062	32	0.00	0.020
33	0.00	0.018	34	0.00	0.002
35	0.00	0.025	36	0.00	0.005
37	0.00	0.028	38	0.00	0.012
39	0.00	0.008	40	0.00	0.005

(c)

FIGURE 9. %THD of (a) phase-A, (b) phase-B, and (c) phase-C current without compensation.

switching pulses in the VSI. DSP generates switching commands, which are sent through its general-purpose input and output ports. These pulses are then isolated by the TLP-250 circuit before being fed to the VSI.

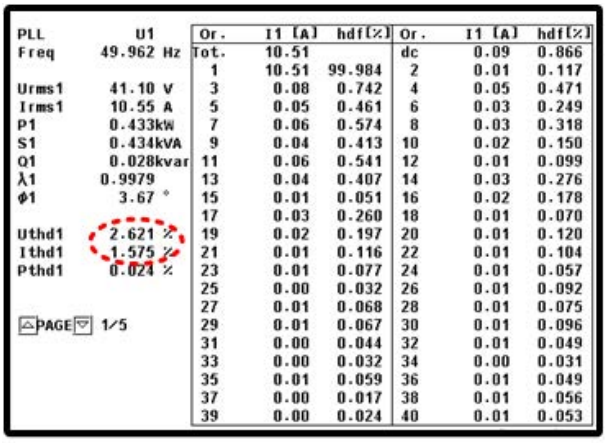

PLL	U1	Or.	I1 [A]	hdf[%]	Or.	I1 [A]	hdf[%]
Freq	49.962 Hz	Tot.	10.51		dc	0.09	0.866
		1	10.51	99.984	2	0.01	0.117
Urms1	41.10 V	3	0.08	0.742	4	0.05	0.471
Irms1	10.55 A	5	0.05	0.461	6	0.03	0.249
P1	0.433kW	7	0.06	0.574	8	0.03	0.318
S1	0.434kVA	9	0.04	0.413	10	0.02	0.150
Q1	0.028kvar	11	0.06	0.541	12	0.01	0.099
λ1	0.9979	13	0.04	0.407	14	0.03	0.276
ϕ1	3.67 °	15	0.01	0.051	16	0.02	0.178
		17	0.03	0.260	18	0.01	0.070
Uthd1	2.621 %	19	0.02	0.197	20	0.01	0.120
Ithd1	1.575 %	21	0.01	0.116	22	0.01	0.104
Pthd1	0.024 %	23	0.01	0.077	24	0.01	0.057
		25	0.00	0.032	26	0.01	0.092
		27	0.01	0.068	28	0.01	0.075
PAGE	1/5	29	0.01	0.067	30	0.01	0.096
		31	0.00	0.044	32	0.01	0.049
		33	0.00	0.032	34	0.00	0.031
		35	0.01	0.059	36	0.01	0.049
		37	0.00	0.017	38	0.01	0.056
		39	0.00	0.024	40	0.01	0.053

(a)

PLL	U1	Or.	I2 [A]	hdf[%]	Or.	I2 [A]	hdf[%]
Freq	49.947 Hz	Tot.	10.44		dc	0.00	0.034
		1	10.44	99.983	2	0.08	0.743
Urms2	39.21 V	3	0.03	0.258	4	0.03	0.283
Irms2	10.38 A	5	0.07	0.624	6	0.02	0.236
P2	0.407kW	7	0.10	0.992	8	0.08	0.731
S2	0.407kVA	9	0.01	0.115	10	0.05	0.456
Q2	0.017kvar	11	0.02	0.194	12	0.02	0.163
λ2	0.9991	13	0.01	0.108	14	0.01	0.052
ϕ2	2.42 °	15	0.03	0.273	16	0.02	0.176
		17	0.04	0.398	18	0.01	0.110
Uthd2	2.567 %	19	0.02	0.177	20	0.01	0.072
Ithd2	1.848 %	21	0.01	0.068	22	0.01	0.092
Pthd2	0.005 %	23	0.01	0.123	24	0.02	0.158
		25	0.01	0.140	26	0.00	0.035
		27	0.01	0.105	28	0.01	0.071
PAGE	2/5	29	0.01	0.123	30	0.00	0.041
		31	0.01	0.086	32	0.00	0.040
		33	0.01	0.051	34	0.00	0.029
		35	0.00	0.031	36	0.00	0.043
		37	0.00	0.018	38	0.00	0.022
		39	0.00	0.033	40	0.00	0.026

(b)

PLL	U1	Or.	I3 [A]	hdf[%]	Or.	I3 [A]	hdf[%]
Freq	50.008 Hz	Tot.	10.21		dc	0.04	0.356
		1	10.21	99.980	2	0.03	0.291
Urms3	39.66 V	3	0.11	1.105	4	0.03	0.259
Irms3	10.18 A	5	0.04	0.364	6	0.05	0.471
P3	0.403kW	7	0.07	0.666	8	0.06	0.602
S3	0.404kVA	9	0.06	0.575	10	0.03	0.314
Q3	0.030kvar	11	0.04	0.387	12	0.04	0.345
λ3	0.9973	13	0.01	0.129	14	0.01	0.112
ϕ3	4.21 °	15	0.03	0.261	16	0.02	0.244
		17	0.02	0.234	18	0.01	0.089
Uthd3	2.385 %	19	0.02	0.163	20	0.02	0.163
Ithd3	1.943 %	21	0.01	0.093	22	0.01	0.084
Pthd3	0.002 %	23	0.03	0.339	24	0.01	0.127
		25	0.02	0.201	26	0.01	0.049
		27	0.01	0.065	28	0.01	0.069
PAGE	3/5	29	0.01	0.126	30	0.01	0.075
		31	0.01	0.117	32	0.01	0.096
		33	0.00	0.002	34	0.01	0.049
		35	0.01	0.075	36	0.00	0.034
		37	0.00	0.048	38	0.00	0.025
		39	0.01	0.055	40	0.00	0.038

(c)

FIGURE 10. %THD of (a) phase-A, (b) phase-B, and (c) phase-C current with compensation.

A. CASE-1

By connecting a rectifier to a restive and inductive load, a three-phase nonlinear load is created. Fig. 8(a) shows the nature of the nonlinear load current. The source provides a nonlinear characteristic current to the load. When

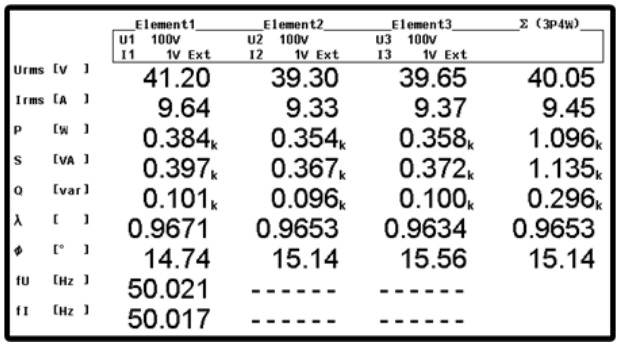

	Element1 U1 100V I1 1V Ext	Element2 U2 100V I2 1V Ext	Element3 U3 100V I3 1V Ext	Σ (3P4W)
Urms [V]	41.20	39.30	39.65	40.05
Irms [A]	9.64	9.33	9.37	9.45
P [W]	0.384k	0.354k	0.358k	1.096k
S [VA]	0.397k	0.367k	0.372k	1.135k
Q [var]	0.101k	0.096k	0.100k	0.296k
λ [ ]	0.9671	0.9653	0.9634	0.9653
ϕ [°]	14.74	15.14	15.56	15.14
fU [Hz]	50.021	------	------	
fI [Hz]	50.017	------	------	

(a)

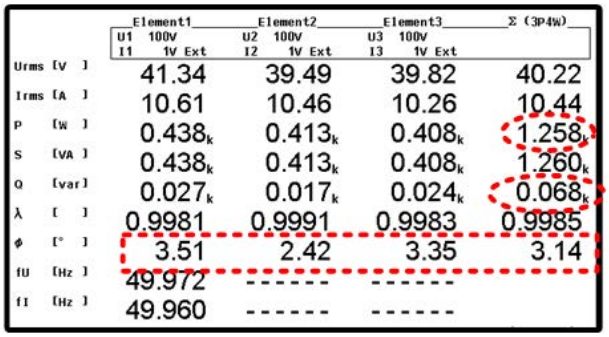

	Element1 U1 100V I1 1V Ext	Element2 U2 100V I2 1V Ext	Element3 U3 100V I3 1V Ext	Σ (3P4W)
Urms [V]	41.34	39.49	39.82	40.22
Irms [A]	10.61	10.46	10.26	10.44
P [W]	0.438k	0.413k	0.408k	1.258k
S [VA]	0.438k	0.413k	0.408k	1.260k
Q [var]	0.027k	0.017k	0.024k	0.068k
λ [ ]	0.9981	0.9991	0.9983	0.9985
ϕ [°]	3.51	2.42	3.35	3.14
fU [Hz]	49.972	------	------	
fI [Hz]	49.960	------	------	

(b)

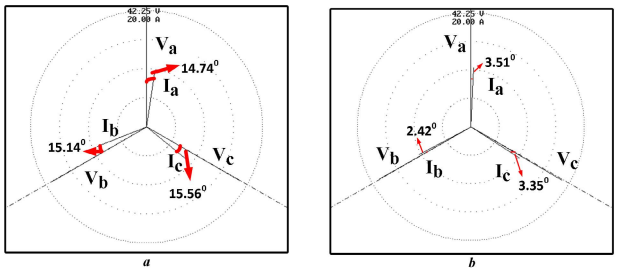

(c)

FIGURE 11. Power flow analysis (a) without, (b) with operation of DSTATCOM; (c) Vector diagram of the system without and with compensation.

DSTATCOM is turned on, the appropriate compensating current is injected from DSTATCOM into the grid at PCC. The compensating harmonic current from DSTATCOM is shown in Fig. 8(b). The grid that is supplying the nonlinear current begins to supply a sinusoidal current, as shown in Fig. 8(c). Fig. 9 illustrates the THD of the load current. Fig. 10 shows the THD of the grid currents of various phases. In these numbers, it is observed that the grid current possesses just the fundamental component of the load demand, indicating that the THD of the grid current has been lowered to 1.57%, 1.84%, and 1.94%, respectively, from 19.48%, 20.60%, and 20.28%. Fig. 11(a) shows the study of the power quality of the grid prior to the operation of the VSC. The grid initially supplies 1.09 KW of active power and 296 vars of reactive power to the load. When the VSC is turned on, the reactive power supplied by the grid drops to 68 vars, as indicated in Fig. 11(b). It is also worth noting that the phase angle between

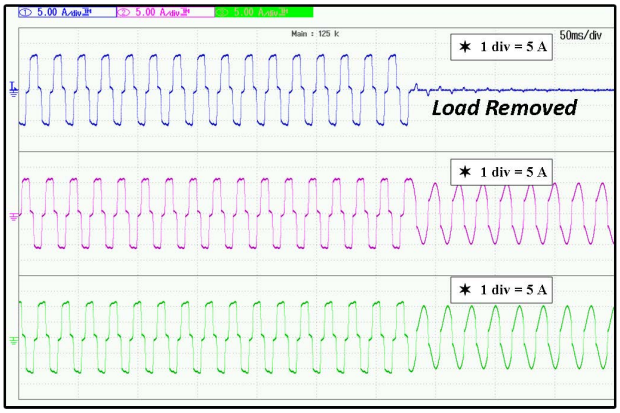

(a)

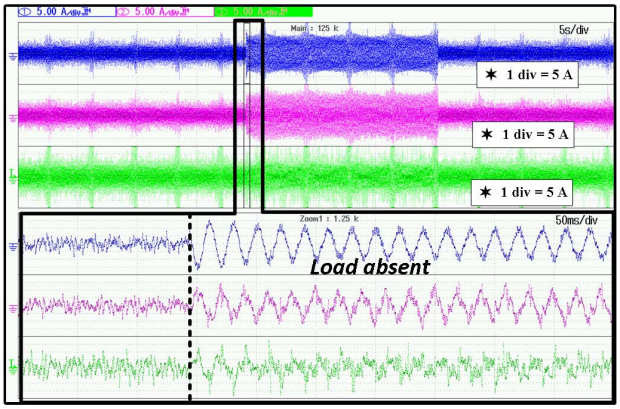

(b)

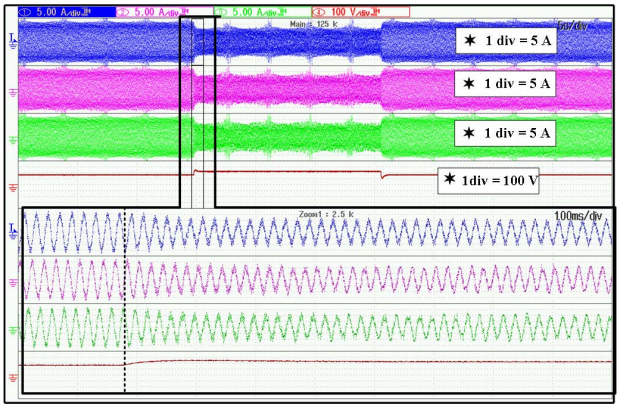

(c)

FIGURE 12. Nonlinear characteristic of (a) current with load removal, (b) Compensation current flow from DSTATCOM, and (c) grid current with the operation of DSTATCOM at transient condition.

the grid voltage and the grid current of different phases has improved and is now close to unity. This suggests that the reliance on the grid for reactive power has decreased significantly. Figure 11(c) depicts a vector diagram of several phases of grid voltage and currents before and after adjustment.

B. CASE-2

To test the algorithm's robustness further, one of the load input phases (A-phase) is deleted. As demonstrated in

PLL	U1	Or.	I1 [A]	hdf[%]	Or.	I1 [A]	hdf[%]
Freq	49.962 Hz	Tot.	6.32		dc	0.09	1.461
		1	6.31	99.922	2	0.04	0.601
Urms1	41.98 V	3	0.12	1.862	4	0.04	0.631
Irms1	6.29 A	5	0.07	1.079	6	0.03	0.490
P1	0.263kW	7	0.08	1.294	8	0.05	0.866
S1	0.264kVA	9	0.08	1.301	10	0.03	0.461
Q1	0.026kvar	11	0.07	1.048	12	0.03	0.471
λ1	0.9951	13	0.04	0.558	14	0.04	0.679
ϕ1	5.65 °	15	0.05	0.743	16	0.03	0.448
		17	0.02	0.385	18	0.02	0.340
Uthd1	1.542 %	19	0.01	0.196	20	0.03	0.418
Ithd1	3.672 %	21	0.01	0.140	22	0.01	0.147
Pthd1	0.001 %	23	0.01	0.116	24	0.01	0.113
		25	0.00	0.072	26	0.01	0.106
		27	0.00	0.079	28	0.00	0.038
PAGE	1/5	29	0.00	0.076	30	0.00	0.019
		31	0.01	0.124	32	0.01	0.096
		33	0.00	0.070	34	0.00	0.079
		35	0.00	0.021	36	0.01	0.082
		37	0.01	0.110	38	0.00	0.057
		39	0.00	0.022	40	0.00	0.006

(a)

PLL	U1	Or.	I2 [A]	hdf[%]	Or.	I2 [A]	hdf[%]
Freq	49.997 Hz	Tot.	6.59		dc	-0.06	-0.953
		1	6.59	99.925	2	0.02	0.362
Urms2	40.14 V	3	0.17	2.621	4	0.01	0.192
Irms2	6.61 A	5	0.07	1.055	6	0.02	0.251
P2	0.264kW	7	0.10	1.443	8	0.06	0.984
S2	0.265kVA	9	0.04	0.659	10	0.03	0.482
Q2	0.030kvar	11	0.02	0.257	12	0.04	0.596
λ2	0.9937	13	0.04	0.672	14	0.02	0.252
ϕ2	6.46 °	15	0.04	0.606	16	0.03	0.427
		17	0.00	0.072	18	0.01	0.150
Uthd2	1.708 %	19	0.01	0.175	20	0.03	0.384
Ithd2	3.744 %	21	0.01	0.174	22	0.01	0.206
Pthd2	0.008 %	23	0.01	0.125	24	0.02	0.259
		25	0.01	0.155	26	0.01	0.134
		27	0.00	0.011	28	0.01	0.082
PAGE	2/5	29	0.01	0.167	30	0.01	0.147
		31	0.01	0.168	32	0.00	0.050
		33	0.01	0.158	34	0.00	0.062
		35	0.00	0.064	36	0.01	0.083
		37	0.00	0.061	38	0.01	0.094
		39	0.01	0.108	40	0.01	0.094

(b)

PLL	U1	Or.	I3 [A]	hdf[%]	Or.	I3 [A]	hdf[%]
Freq	49.968 Hz	Tot.	6.25		dc	-0.01	-0.089
		1	6.24	99.876	2	0.10	1.655
Urms3	40.13 V	3	0.17	2.735	4	0.04	0.594
Irms3	6.32 A	5	0.18	2.900	6	0.08	1.238
P3	0.252kW	7	0.05	0.728	8	0.02	0.333
S3	0.254kVA	9	0.07	1.119	10	0.04	0.630
Q3	0.029kvar	11	0.05	0.730	12	0.02	0.288
λ3	0.9933	13	0.03	0.560	14	0.01	0.104
ϕ3	6.65 °	15	0.03	0.425	16	0.02	0.383
		17	0.03	0.483	18	0.01	0.201
Uthd3	2.656 %	19	0.01	0.190	20	0.02	0.352
Ithd3	4.985 %	21	0.01	0.187	22	0.01	0.238
Pthd3	0.002 %	23	0.01	0.170	24	0.01	0.128
		25	0.01	0.217	26	0.00	0.067
		27	0.01	0.127	28	0.01	0.130
PAGE	3/5	29	0.01	0.094	30	0.00	0.034
		31	0.00	0.032	32	0.00	0.031
		33	0.01	0.115	34	0.01	0.091
		35	0.01	0.087	36	0.01	0.101
		37	0.00	0.048	38	0.01	0.101
		39	0.00	0.022	40	0.00	0.008

(c)

FIGURE 13. %THD of (a) phase-A, (b) phase-B, and (c) phase-C current with compensation during transient period.

Fig. 12(a), the three-phase nonlinear load is reduced to a single-phase nonlinear load. As the demand for the nonlinear load current decreased, so did the compensation current drawn from DSTATCOM, as illustrated in Fig. 12(b). The compensatory current in phase A becomes virtually

	Element1	Element2	Element3	Σ (3P4W)
	U1 100V I1 1V Ext	U2 100V I2 1V Ext	U3 100V I3 1V Ext	
Urms [V]	41.66	39.89	40.22	40.59
Irms [A]	6.26	6.52	6.31	6.36
P [W]	0.260k	0.258k	0.252k	0.770k
S [VA]	0.261k	0.260k	0.254k	0.775k
Q [var]	0.025k	0.030k	0.029k	0.084k
λ [ ]	0.9955	0.9934	0.9935	0.9941
φ [°]	5.47	6.60	6.55	6.22
fU [Hz]	49.969	------	------	
fI [Hz]	50.004	------	------	

FIGURE 14. Power flow analysis of the system with compensation during transient operation.

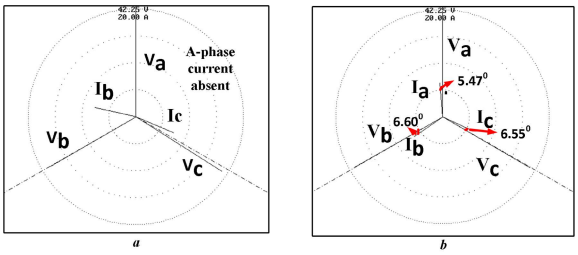

FIGURE 15. Vector diagram of the system (a) without compensation, (b) with compensation during transient operation.

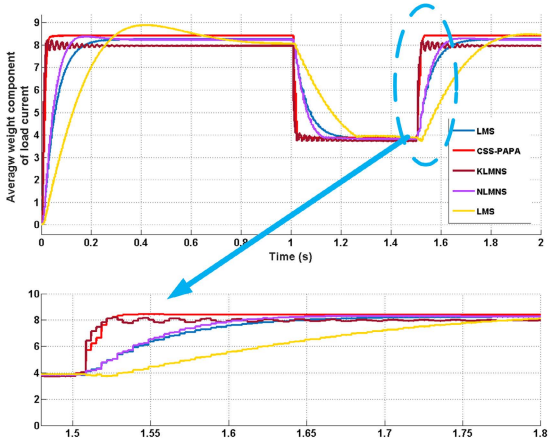

FIGURE 16. Comparative analysis of the proposed theory with other adaptive theory.

sinusoidal. However, the remaining two phases of DSTATCOM give the necessary amount of reactive power to the system. The grid currents are sinusoidal during the transient situation, as seen in Fig. 12(c). As illustrated in Fig. 12(b), the dc-link voltage increases from 169 V to 222 V to enable the correction of reactive power during the transient condition. The compensatory power is injected into the system so that, during transient conditions, the THD in all three phases of the grid current is 3.6%, 3.7%, and 4.9%, as shown in Fig. 13. Fig. 14 depicts the power flow analysis. During a malfunctioning situation, the grid can only support 89 vars. It is also worth noting that VSC continues to infuse power into the system even when the load demand decreases. As a result, excess electricity is fed back into the grid. The grid has an A-phase current with amplitude identical to the other two phases, as shown in Fig. 12(c), even though there is no load demand in that phase. The phase angle improved during the defective state, as seen in Fig. 15. However, once they began, they became balanced and the same magnitude in phase with the phase voltage. This is obvious and can be seen from the wave shape of the critical component to correct for the unbalance. As a result, it was boosted (as seen by the unbalance; as a result, it got larger after starting), resulting in a waveform that is balanced with the other two phases. Fig. 15 shows the waveform of the fundamental component of the load current retrieved by CSS-PAPA control theory and other adaptive control theories when exposed to the same system condition and rating. According to Fig. 8(c), the oscillation is reduced in the suggested theory during the extraction of fundamental signals. Again, in comparison to the proposed hypothesis, oscillations increase during transitory conditions and take longer to stabilize.

C. COMPARATIVE STUDY

This is proven in Fig. 16 by comparing the performance of the proposed CSS-PAPA control algorithm and other adaptive ways to extract the fundamental component of the load current in equal ratings under equivalent scenarios. The proposed CSS-PAPA method to extract the basic signal provides a fast response and reduced oscillations compared to LMS [27], KLMNS [28], NLMS [29] and RLS [30]. In this study, it is found that LMS had a much slower convergence rate than other adaptive filters in both steady and transient states. RLS and NLMS operate similarly under transient conditions. Improved performance in terms of error tracking and convergence speed has been reported using the KLMNS filter. Meanwhile, a large oscillation is observed in the initial period, which is not acceptable for industrial applications. The adaptive filter maintains a balance between oscillation and convergence speed. As a result, the suggested CSS-PAPA control algorithm has lesser oscillations and takes less time to stabilize in the transient state condition than the adaptive control of the three methods mentioned above.

IV. CONCLUSION

A control algorithm based on the CSS-PAPA algorithm has been developed for reducing THD in the grid current reactive sharing in the DSTATCOM to reduce the dependency on the grid. Extensive test results have been presented backed with simulation results for the proposed control algorithm. The control algorithm has been developed and implemented to generate switching pulses for VSC. An excellent performance has been noticed for the CSS-PAPA algorithm compared to the conventional adaptive filter. In terms of convergence speed, harmonic compensation, error minimization, and computational complexity. The experimental results show that the proposed control algorithm works well under closed-loop

conditions with steady state as well as dynamic loading condition. The advantage of CSS-PAPA is the separation of the fundamental and higher-order harmonic components of the polluted current precisely without any magnitude reduction and phase delay. In this proposed work, reactive power is driven into the grid as compensation during steady-state and transient-state. In this paper, the elicitation of fundamental components and detection of harmonics without PLL are presented. This method eliminates the delay attached to different filters and solves the influence of PLL detection accurately increasing the speed of the dynamics response. It is observed that the THD of the grid current is satisfying the IEEE-519 standard. It is also cognized that VSC not only penetrates energy into the grid, but also decreases the harmonics of the load currents. The test results have corroborated the authenticity of the proposed controller.

REFERENCES

[1] M. A. Awal, L. Della Flora, and I. Husain, "Observer based generalized active damping for voltage source converters with LCL filters," *IEEE Trans. Power Electron.*, vol. 37, no. 1, pp. 125–136, Jan. 2022.

[2] J. Zhuo, C. An, and J. Fei, "Fuzzy multiple hidden layer neural sliding mode control of active power filter with multiple feedback loop," *IEEE Access*, vol. 9, pp. 114294–114307, 2021.

[3] W.-K. Sou, C.-W. Chao, C. Gong, C.-S. Lam, and C.-K. Wong, "Analysis, design, and implementation of multi-quasi-proportional-Resonant controller for thyristor-controlled LC-coupling hybrid active power filter (TCLC-HAPF)," *IEEE Trans. Ind. Electron.*, vol. 69, no. 1, pp. 29–40, Jan. 2022.

[4] L. Vetoshkin and Z. Müller, "Dynamic stability improvement of power system by means of STATCOM with virtual inertia," *IEEE Access*, vol. 9, pp. 116105–116114, 2021.

[5] L. L. de Souza, N. Rocha, D. A. Fernandes, R. P. R. de Sousa, and C. B. Jacobina, "Grid harmonic current correction based on parallel three-phase shunt active power filter," *IEEE Trans. Power Electron.*, vol. 37, no. 2, pp. 1422–1434, Feb. 2022.

[6] R. Kumar, B. Singh, and D. T. Shahani, "Symmetrical components-based modified technique for power-quality disturbances detection and classification," *IEEE Trans. Ind. Appl.*, vol. 52, no. 4, pp. 3443–3450, Jul./Aug. 2016.

[7] P. D. Achlerkar and B. K. Panigrahi, "New perspectives on stability of decoupled double synchronous reference frame PLL," *IEEE Trans. Power Electron.*, vol. 37, no. 1, pp. 285–302, Jan. 2022.

[8] B. Hu, H. Nian, J. Yang, M. Li, and Y. Xu, "High-frequency resonance analysis and reshaping control strategy of DFIG system based on DPC," *IEEE Trans. Power Electron.*, vol. 36, no. 7, pp. 7810–7819, Jul. 2021.

[9] R. S. Herrera, P. SalmerÓn, and H. Kim, "Instantaneous reactive power theory applied to active power filter compensation: Different approaches, assessment, and experimental results," *IEEE Trans. Ind. Electron.*, vol. 55, no. 1, pp. 184–196, Jan. 2008.

[10] M. T. Ahmad, N. Kumar, and B. Singh, "AVSF-based control algorithm of DSTATCOM for distribution system," *IET Gener., Transmiss. Distribution*, vol. 11, no. 13, pp. 3389–3396, Sep. 2017.

[11] M. Qasim, P. Kanjiya, and V. Khadkikar, "Optimal current harmonic extractor based on unified ADALINEs for shunt active power filters," *IEEE Trans. Power Electron.*, vol. 29, no. 12, pp. 6383–6393, Dec. 2014.

[12] M. H. Haque and P. Kumkratug, "Application of Lyapunov stability criterion to determine the control strategy of a STATCOM," *IEE Proc., Gener., Transmiss. Distrib.*, vol. 151, no. 3, pp. 415–420, May 2004.

[13] B. Singh, S. R. Arya, A. Chandra, and K. Al-Haddad, "Implementation of adaptive filter in distribution static compensator," *IEEE Trans. Ind. Appl.*, vol. 50, no. 5, pp. 3026–3036, Sep. 2014.

[14] K. Venkatraman, M. P. Selvan, and S. Moorthi, "Predictive current control of distribution static compensator for load compensation in distribution system," *IET Gener., Transmiss. Distrib.*, vol. 10, no. 10, pp. 2410–2423, Jul. 2016.

[15] R. Kumar, B. Singh, D. T. Shahani, and C. Jain, "Dual-tree complex wavelet transform-based control algorithm for power quality improvement in a distribution system," *IEEE Trans. Ind. Electron.*, vol. 64, no. 1, pp. 764–772, Jan. 2017.

[16] R. Panigrahi, B. Subudhi, and P. C. Panda, "A robust LQG servo control strategy of shunt-active power filter for power quality enhancement," *IEEE Trans. Power Electron.*, vol. 31, no. 4, pp. 2860–2869, Apr. 2016.

[17] S. P. Gawande, M. R. Ramteke, and N. Pande, "Improved equal current approach for reference current generation in shunt applications under unbalanced and distorted source and load conditions," *IET Gener., Transmiss. Distrib.*, vol. 10, no. 4, pp. 995–1005, Mar. 2016.

[18] P. Chittora, A. Singh, and M. Singh, "Gauss–Newton-based fast and simple recursive algorithm for compensation using shunt active power filter," *IET Gener., Transmiss. Distrib.*, vol. 11, no. 6, pp. 1521–1530, Apr. 2017.

[19] M. Badoni, A. Singh, and B. Singh, "Comparative performance of Wiener filter and adaptive least mean square-based control for power quality improvement," *IEEE Trans. Ind. Electron.*, vol. 63, no. 5, pp. 3028–3037, May 2016.

[20] A. Dash, D. P. Bagarty, P. K. Hota, R. K. Behera, U. R. Muduli, and K. Al Hosani, "DC-offset compensation for three-phase grid-tied SPV-DSTATCOM under partial shading condition with improved PR controller," *IEEE Access*, vol. 9, pp. 132215–132224, 2021.

[21] A. Dash, D. P. Bagarty, P. K. Hota, U. R. Muduli, K. A. Hosani, and R. K. Behera, "Performance evaluation of three-phase grid-tied SPV-DSTATCOM with DC-offset compensation under dynamic load condition," *IEEE Access*, vol. 9, pp. 161395–161406, 2021.

[22] Z. X. Zou, K. Zhou, Z. Wang, and M. Cheng, "Frequency-adaptive fractional-order repetitive control of shunt active power filters," *IEEE Trans. Ind. Electron.*, vol. 62, no. 3, pp. 1659–1668, Mar. 2015.

[23] G. Pathak, B. Singh, and B. K. Panigrahi, "Control of wind-diesel microgrid using affine projection-like algorithm," *IEEE Trans. Ind. Informat.*, vol. 12, no. 2, pp. 524–531, Apr. 2016.

[24] M. Badoni, B. Singh, and A. Singh, "Implementation of echo-state network-based control for power quality improvement," *IEEE Trans. Ind. Electron.*, vol. 64, no. 7, pp. 5576–5584, Jul. 2017.

[25] J.-M. Song and P. Park, "An optimal variable step-size affine projection algorithm for the modified filtered-x active noise control," *Signal Process.*, vol. 114, pp. 100–111, Sep. 2015.

[26] F. Huang, J. Zhang, and S. Zhang, "Combined-step-size affine projection sign algorithm for robust adaptive filtering in impulsive interference environments," *IEEE Trans. Circuits Syst. II, Exp. Briefs*, vol. 63, no. 5, pp. 493–497, May 2016.

[27] A. Kumar and P. Kumar, "Power quality improvement for grid-connected PV system based on distribution static compensator with fuzzy logic controller and UVT/ADALINE-based least mean square controller," *J. Modern Power Syst. Clean Energy*, vol. 9, no. 6, pp. 1289–1299, 2021.

[28] U. R. Muduli and K. Ragavan, "Dynamic modeling and control of shunt active power filter," in *Proc. 18th Nat. Power Syst. Conf. (NPSC)*, Dec. 2014, pp. 1–6.

[29] B. K. Das, G. V. Chakravarthi, and M. Chakraborty, "A convex combination of NLMS and ZA-NLMS for identifying systems with variable sparsity," *IEEE Trans. Circuits Syst. II, Exp. Briefs*, vol. 64, no. 9, pp. 1112–1116, Sep. 2017.

[30] K. Zhu, C. Yu, and Y. Wan, "Recursive least squares identification with variable-direction forgetting via oblique projection decomposition," *IEEE/CAA J. Automatica Sinica*, vol. 9, no. 3, pp. 547–555, Mar. 2022.

[31] M. I. Marei, E. F. El-Saadany, and M. M. A. Salama, "A novel control scheme for STATCOM using space vector modulation based hysteresis current controller," in *Proc. 11th Int. Conf. Harmon. Quality Power*, Sep. 2004, pp. 58–65.

[32] M. I. Marei, E. F. El-Saadany, and M. M. A. Salama, "A flexible DG interface based on a new RLS algorithm for power quality improvement," *IEEE Syst. J.*, vol. 6, no. 1, pp. 68–75, Mar. 2012.

[33] M. I. Marei, E. F. El-Saadany, and M. M. A. Salama, "Dynamic performance of an enhanced STATCOM current control scheme for reactive power compensation," in *Proc. Can. Conf. Electr. Comput. Eng. Toward Caring Humane Technol. (CCECE)*, May 2003, pp. 359–362.

[34] Z. Shu, N. Ding, J. Chen, H. Zhu, and X. He, "Multilevel SVPWM with DC-link capacitor voltage balancing control for diode-clamped multilevel converter based STATCOM," *IEEE Trans. Ind. Electron.*, vol. 60, no. 5, pp. 1884–1896, May 2013.

[35] M. B. Shadmand, M. Mosa, R. S. Balog, and H. Abu-Rub, "Model predictive control of a capacitorless matrix converter-based statcom," *IEEE J. Emerg. Sel. Topics Power Electron.*, vol. 5, no. 2, pp. 796–808, Jun. 2017.

[36] S. Vazquez, A. Marquez, R. Aguilera, D. Quevedo, J. I. Leon, and L. G. Franquelo, "Predictive optimal switching sequence direct power control for grid-connected power converters," *IEEE Trans. Trans. Ind. Electron.*, vol. 62, no. 4, pp. 2010–2020, Mar. 2015.
[37] J. Segundo-Ramirez and A. Medina, "Modeling of FACTS devices based on SPWM VSCs," *IEEE Trans. Power Del.*, vol. 24, no. 4, pp. 1815–1823, Oct. 2009.
[38] J. K. Singh, K. A. Jaafari, R. K. Behera, K. A. Hosani, and U. R. Muduli, "Faster convergence controller with distorted grid conditions for photovoltaic grid following inverter system," *IEEE Access*, vol. 10, pp. 29834–29845, 2022.

AROBINDA DASH (Graduate Student Member, IEEE) received the B.Tech. and M.Tech. degrees in electrical engineering from the Biju Patnaik University of Technology, Rourkela, Odisha, India, and the Ph.D. degree in electrical engineering from the College of Engineering and Technology, Bhubaneswar, Odisha, in 2022. He is currently working as a Research Intern with the Department of Electrical Engineering, Indian Institute of Technology Patna, India. His research interests include phase-locked loops, power electronics convertor and its application to power systems, power system harmonics, renewable energy integration, and grid synchronization.

UTKAL RANJAN MUDULI (Member, IEEE) received the B.Tech. degree in electrical and electronics engineering from the Biju Patnaik University of Technology, Rourkela, Odisha, India, in 2011, the M.Tech. degree in electrical engineering from the Indian Institute of Technology Gandhinagar, India, in 2014, and the Ph.D. degree in electrical engineering from the Indian Institute of Technology Patna, India, in 2022. He was a Visiting Scholar and a Research Associate with the Department of Electrical Engineering and Computer Science, Khalifa University, United Arab Emirates, in 2019 and 2021, respectively, where he is currently working as a Postdoctoral Research Fellow. His research interests include modulation strategies for multiphase motor drives, matrix converters and its control, battery power management, and wireless power transfer.

SURYA PRAKASH (Graduate Student Member, IEEE) received the B.Tech. degree in electrical and electronics engineering from JNTUH Hyderabad, India, in 2009, and the M.Tech. degree in power electronics engineering from VNIT Nagpur, Maharashtra, in 2012. He is currently a Research Scholar with the Department of Electrical Engineering, Indian Institute of Technology (IIT) Patna, Bihar, India. His research interests include control methods for power electronics converters in distribution systems and renewable energy resources, grid interconnection issues, power quality enhancement, and low-voltage ride-through.

KHALIFA AL HOSANI (Senior Member, IEEE) received the B.Sc. and M.Sc. degrees in electrical engineering from the University of Notre Dame, Notre Dame, IN, USA, in 2005 and 2007, respectively, and the Ph.D. degree in electrical and computer engineering from The Ohio State University, Columbus, OH, USA, in 2011. He is currently an Associate Professor with the Department of Electrical and Computer Engineering, Khalifa University, Abu Dhabi, United Arab Emirates. He is the Co-Founder of the Power Electronics and Advanced Sustainable Energy Center Laboratory, ADNOC Research and Innovation Center, Abu Dhabi. His research interests include a wide range of topics, including nonlinear control, sliding mode control, control of power electronics, power systems stability and control, renewable energy systems modeling and control, smart grid, microgrid and distributed generation, and application of control theory to oil and gas applications.

SANDHYA RANI GONGADA received the B.Tech. degree in electrical and electronics engineering from Acharya Nagarjuna University, India, in 2000, and the M.Tech. degree in electrical power engineering from Jawaharlal Nehru Technological University Hyderabad, India, in 2008. She is currently pursuing the Ph.D. degree with Osmania University, Hyderabad. She has 20 years of teaching experience in various institutes and is currently working as an Assistant Professor with the Department of Electrical and Electronics Engineering, Vasavi College of Engineering, Hyderabad. Her research interests include neural networks and its application to power systems, machine learning and IoT, microprocessors, and microcontrollers.

RANJAN KUMAR BEHERA (Senior Member, IEEE) received the B.Eng. degree in electrical engineering from the Regional Engineering College (NIT) Rourkela, India, in 1998, and the M.Tech. and Ph.D. degrees from the Indian Institute of Technology Kanpur, India, in 2003 and 2009, respectively. He was a Visiting Scholar with the Energy Systems Research Center, Tennessee Technological University, USA, in 2008. He has been a Faculty Member (since 2009) and is currently an Associate Professor with the Department of Electrical Engineering, Indian Institute of Technology Patna, India. In July 2016, he was a Visiting Research Collaborator with the Department of Electrical, Electronic and Computer Engineering, University of Pretoria, South Africa. His research interests include nonlinear control theory applications to power electronic converters, pulse width modulation techniques, and multiphase electric drive control. He has received many national and international awards, such as the Young Scientists Award in engineering sciences, DST, Government of India, in 2001; the Bhaskara Advanced Solar Energy (BASE) Indo-U.S. Science and Technology Forum for Solar research in the USA, in 2014; and selected as the featured engineer of the globe, in 2015.